Industrial Crops & Products 234 (2025) 121596

Contents lists available at ScienceDirect

Industrial Crops & Products

journal homepage: www.elsevier.com/locate/indcrop

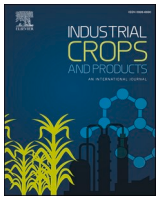

Engineered biochar with MgO impregnation: A phosphorus vector bridging aquatic systems and agricultural soils via targeted adsorption and controlled release

Meiling Zhang [a,1], Yu Li [b,c,1], Shuang Ai [a,b], Xianghui Meng [a,b], Jianghao Cheng [a,b], Zhuqing Liu [b,c], Fan Yang [b,c], Kui Cheng [a,b,*]

[a] College of Engineering, Northeast Agricultural University, Harbin, China
[b] International Cooperation Joint Laboratory of Health in Cold Region Black Soil Habitat of the Ministry of Education, China
[c] School of Water Conservancy and Civil Engineering, Northeast Agricultural University, Harbin, China

ARTICLE INFO

Keywords:
MgO-Biochar
Phosphorus sorption
Desorption
Chemical foaming strategy
Slow-release fertilizer

ABSTRACT

The global community is confronted with two interconnected issues: phosphorus contamination in water bodies and the diminishing reserves of phosphate rock. This research presents an innovative dual-purpose strategy, which utilizes MgO-modified biochar (MgO-BC) to extract phosphorus from wastewater and subsequently recycle it into a controlled-release fertilizer. MgO-BC was synthesized using a chemical foaming strategy, with corn stalk as a carbon precursor and $Mg(HCO_3)_2$ as both an activation agent and metal source, resulting in a honeycomb-like MgO-modified biochar. The phosphorus adsorption onto MgO-modified biochar (MgO-BC) adhered to pseudo-second-order kinetics, achieving a maximum adsorption capacity of 189.90 mg/g, suggesting that chemical processes predominantly govern phosphorus capture. The primary mechanisms for phosphorus removal by MgO-BC are electrostatic interactions and complexation reactions. Field and laboratory tests demonstrated that MgO-BC-P_{ads} effectively released 59.02 % of the absorbed phosphorus into the soil within 35 days. Moreover, compared to the CK group, the MgO-BC-P_{ads} treatment significantly increased the dry weight (131.58 %), leaf length (14.37 %), and leaf number (57.14 %) of the bok choy. It also enhanced root length (52.24 %) and surface area (76.39 %) compared to the superphosphate treatment (CF). This research highlights the potential of MgO-BC as a viable and sustainable approach for waste management and agricultural enhancement.

1. Introduction

Phosphorus plays a crucial role in agriculture as a vital nutrient for plant growth and food production (Cordell et al., 2009; Reinhard et al., 2017). However, due to its reactive nature, over 80 % of applied phosphorus fertilizers become unavailable for plant uptake through sorption processes or microbial immobilization. Annually, around 15 million tons of phosphorus fertilizer are applied to fulfill plant phosphorus needs, yet only 5–30 % is absorbed by crops (Wang et al., 2012; Zhu et al., 2018). Excess phosphorus that fails to re-enter the biogeochemical cycle contaminates water bodies, causing harmful algal blooms, water quality degradation, and disruption of aquatic ecosystems (Huang et al., 2024). In China, agriculture phosphorus losses were estimated at approximately 76.2 Mt in 2017, surpassing losses from industrial sources (70.9 Mt) (Cao et al., 2014). At the same time, phosphate rock is a finite, non-renewable resource, with global reserves being depleted at an alarming and uneven rate. The US Geological Survey estimates that approximately 62 billion tonnes of phosphate remain in the earth, which could be exhausted within the next 300 years (Gilbert, 2009; Peng et al., 2023). Therefore, developing technologies to recover phosphorus from wastewater and recycle it into soil is crucial for controlling phosphorus pollution and mitigating the depletion of phosphate rock resources.

Previously reported methods for addressing phosphorus pollution in wastewater include biological processes (Chen et al., 2022; Izadi et al., 2020), chemical precipitation (Ma et al., 2021; Piash et al., 2022), ion exchange (Guida et al., 2021; Ownby et al., 2021), and adsorption (Bacelo et al., 2020; Dai et al., 2020). Among these, adsorption stands out as a promising alternative, enabling both phosphate removal and

* Corresponding author at: College of Engineering, Northeast Agricultural University, Harbin, China.
E-mail address: chengkui@neau.edu.cn (K. Cheng).
[1] These authors contribute equally.

https://doi.org/10.1016/j.indcrop.2025.121596
Received 25 February 2025; Received in revised form 25 June 2025; Accepted 23 July 2025
Available online 29 July 2025

recovery (He et al., 2022; Jiao et al., 2021; Zhang et al., 2022). Biochar, a charcoal-like material produced from waste biomass through slow pyrolysis, is commonly used as an adsorbent due to its availability, high surface area, and porous structure (Xiang et al., 2020; Zhou et al., 2021). Furthermore, biochar has shown significant improvements in soil fertility, land restoration, and nutrient use efficiency, thereby enhancing crop productivity (Joseph et al., 2021; Zhang et al., 2021). As a result, phosphorus-absorbing biochar holds significant potential as a slow-release fertilizer, enhancing soil fertility, stimulating crop growth, and boosting agricultural yields (Almanassra et al., 2021; Li et al., 2020; Wang et al., 2020). However, since the primary forms of phosphate in water are $H_2PO_4^-$ and HPO_4^{2-}, pristine biochar, like most carbon-based adsorbents, typically has a negatively charged surface, limiting its ability to adsorb large quantities of anionic phosphate species. Numerous studies have shown that metal cations (such as Ca^{2+}, Fe^{3+}, Mg^{2+}, Al^{3+}, and La^{3+})-modified biochar exhibit a strong affinity for phosphorus recovery (Chen et al., 2020; Hu et al., 2023; Luo et al., 2023; Shakoor et al., 2021). For instance, Zhu et al. (Zhu et al., 2020) created MgO-biochar by pyrolyzing $MgCl_2$-impregnated corn stover, effectively removing and recovering phosphate from aqueous solutions. They observed that adsorption performance improved with increased Mg content, correlating strongly with external surface area. Unlike high-valence metals (e.g., La^{3+}, Al^{3+}), which form insoluble phosphate complexes limiting phosphorus bioavailability, Mg^{2+} generates plant-available struvite analogs crucial for agronomic value creation. Environmentally, MgO hydrolysis yields only benign $Mg(OH)_2$, eliminating ecotoxic risks from leached metal ions. Despite advances in metal-impregnated modified biochar, significant research gaps persist. Optimizing metal ion distribution and the pore structure during impregnation and calcination is crucial, as adsorption capacity correlates with the specific surface area (SSA), providing more adsorption sites. These gaps underscore the necessity for additional studies focused on improving the efficiency of metal infusion into biomass and evaluating its effects on the physical and chemical characteristics of the host materials.

Building on the flour-making process, this research introduces a novel chemical foaming approach to create honeycomb-structured MgO-modified biochar. Corn stalks serve as the carbon source, and Mg $(HCO_3)_2$ acts both as an activation agent and a metal precursor. Crucially, $Mg(HCO_3)_2$'s staged thermal decomposition orchestrates simultaneous pore-engineering and metal dispersion: its low-temperature breakdown (50–350°C) liberates endogenous CO_2 that acts as a nano-porogen to expand hierarchical micro/mesopores, while subsequent $MgCO_3$-to-MgO conversion at 750°C exploits early-released CO_2 as kinetic barriers to confine MgO nanocrystals within the carbon lattice. This intrinsic foaming mechanism transforms the composite into a multifunctional platform for phosphorus recovery-reuse synergy—efficiently capturing aqueous phosphate via MgO ligand exchange and gradually releasing it into soil as a slow-release fertilizer. Through laboratory and field experiments, the main objectives are to, (1) describe the physical and chemical characteristics of MgO-impregnated biochar (MgO-BC) synthesized through the chemical foaming method, (2) investigate the efficacy and mechanisms of MgO-BC in capturing phosphorus from wastewater, (3) examine the release behavior of phosphorus-loaded MgO-BC, (4) evaluate the impact of applying phosphorus-loaded MgO-BC on crop productivity. Ultimately, this research emphasizes the potential of MgO-BC as a multifunctional material that integrates waste management with nutrient recycling within a circular economy framework, thereby promoting environmental sustainability and agricultural resilience.

2. Materials and methods

2.1. Raw material

Corn straw harvested from Northeast Agricultural University's experimental station (Harbin, 45.75°N, 126.53°E) were processed through sequential washing, oven-drying (60°C), and mechanical milling to < 0.18 mm particulates. Experimental soils collected from surface horizons (0–20 cm depth) at the same site underwent standardized homogenization for column leaching and potting experiments. Comprehensive physicochemical characterization data are provided in Supporting Information Table S1.

2.2. Synthesis of Mg-modified biochar (MgO-BC-x)

Pretreated maize stalk particulates were subjected to $Mg(HCO_3)_2$ immersion at varying concentrations (0.1, 0.5, 1.0 M) with 1:1.5 solid-liquid ratio (w/v), followed by continuous agitation (300 rpm, 24 h). The Mg^{2+}-impregnated biomass was oven-dried (60°C, 24 h) prior to pyrolysis treatment. Thermal conversion was conducted in a tubular furnace under argon atmosphere (flow rate 150 mL/min), where 20 g precursor underwent programmed heating (10 °C/min ramp to 750°C, 2 h dwell) to ensure complete transformation of Mg species to highly crystalline MgO while maintaining optimal pore structure. The resultant MgO-biochar variants, designated MgO-BC-(1−3), corresponded to initial $Mg(HCO_3)_2$ concentrations 0.1–1.0 M respectively.

2.3. Batch adsorption experiment, kinetic, and isotherm

The adsorption capacity was determined using the Eq. 1 (Ma et al., 2020).

where q_e (mg/g) represents the equilibrium adsorption capacity, V (L) denotes the solution volume, C_1 (mg/L) and C_2 (mg/L) indicate the initial concentration and the remaining solution concentrations, respectively, and m (g) is the mass of MgO-BC-x.

Kinetic trials employed 0.10 ± 0.01 g/L MgO-BC-x dosage in 10 mg/L PO_4^{3-} solution. Temporal adsorption profiles were monitored over 0–1440 min, with *Pseudo-first-order* (Eq. 2), *Pseudo-second-order* kinetics (Eq. 3), *Elovich* kinetics (Eq. 4) and W&M kinetics (Eq. 5) models applied to interpret the kinetic dataset (Wang and Guo, 2020).

In the isotherm experiments, MgO-BC-x was used at a dosage of 0.10 ± 0.01 g/L, with PO_4^{3-} concentrations ranging from 10 to 120 mg/L. The q_e of MgO-BC for PO_4^{3-} was analyzed using the *Langmuir* (Eq. 6), *Freundlich* (Eq. 7), and *Tempkin* (Eq. 8). Details of the model parameters can be found in the supplementary materials (Liang et al., 2022).

To assess practical applicability of phosphate removal using real wastewater was conducted. Phosphate-contaminated agricultural wastewater was collected from a livestock farm in Harbin, China. The phosphate concentration in the wastewater was 2.33 mg/L.

2.4. Release kinetics of phosphate

Saturated adsorbents were prepared by exposing MgO-BC to 100 mL of 5000 mg/L phosphate solution. Post-equilibrium, materials were rinsed with ultrapure water, oven-dried (105°C, 24 h), and designated MgO-BC-P_{ads}. The saturated adsorbent demonstrated 99.38 mg/g phosphate loading capacity prior to release trials. The phosphate release kinetics of MgO-BC-P_{ads} were studied in deionized water. Specifically, 0.05 g of MgO-BC-P_{ads} and 50 mL of deionized water were added into a conical flask, which was then oscillated at 180 rpm in a thermostatic oscillator set to 25 ± 0.3 °C. The supernatants were collected at various time intervals (0.25, 1, 5, 15, 30, 60, 90, 120, 240, and 360 mins) using 0.45 μm membrane filters. Triplicated experimental sets were analyzed using four transport-kinetic models to decipher MgO-BC-P_{ads}' phosphate liberation pathways: *zero-order model* (Eq. 9), *first-order model* (Eq. 2), *Ritger-Peppas model* (Eq. 10), and *Higuchi model* (Eq. 11) (Zhang et al., 2023).

2.5. Soil column leaching test

The phosphate liberation dynamics of MgO-BC-P_{ads} under

pedospheric conditions were evaluated through standardized soil-column leaching assays. The experimental setup included three treatment groups, CK (control with zero phosphate), CF (superphosphate at 6.66 g/kg, PO_4^{3-} at 1 g/kg), and MgO-BC-P_{ads} (slow-release fertilizer at 10 g/kg, PO_4^{3-} at 0.99 g/kg) (Gao et al., 2023). The experimental columns (10 cm diameter × 30 cm height) were constructed using a dual-layer 135-mesh nylon filtration base, overlaid with a 50 g quartz sand matrix as a drainage medium. Following standardized protocols, pre-processed soil (air-dried, 170 g) was homogeneously blended with respective fertilizer treatments prior to column packing, achieving consistent soil matrix conditions at 1.3 g/cm³ bulk density through controlled mass-volume ratios. An additional 50 g quartz sand was placed at the top of each column to stabilize the soil surface during the leaching process. A schematic diagram of this setup is provided in Fig. S1. After preparing the soil columns, they were watered to 70 % of field capacity and incubated at 25 °C. The leaching process involved adding 240 mL of distilled water to each column on days 7, 14, 21, 28 and 35 to simulate rainfall events and quantify phosphate leaching.

2.6. Pot experiment

Pot experiments with bok choy were conducted in a greenhouse to evaluate the effectiveness of different phosphorus treatments. Three treatment groups were established, CK (control with zero phosphate), CF (superphosphate at 6.66 g/kg), and MgO-BC-P_{ads} (Slow-release fertilizer at 10 g/kg). All treatments were supplemented with identical amounts of nitrogen and potassium. Each treatment was replicated 18 times. Phosphorus release was monitored from both the surface layer and the rhizosphere soil on days 7, 14, 21, 28, and 35 days after sowing. Harvest-stage agronomic metrics (plant height, biomass accumulation (fresh/dry weight) of the bok choy were systematically quantified using standardized protocols. These measures were used to evaluate the impact of the phosphorus treatments on plant growth and development.

2.7. Characterization of MgO-BC-x and soil

The microstructural features of MgO-BC-x composites were analyzed using field emission scanning electron microscopy coupled with energy-dispersive X-ray spectroscopy (FE-SEM/EDS, SU8010, JEOL). This integrated characterization approach enabled simultaneous topographical examination and surface elemental mapping. Field emission transmission electron microscopy (FE-TEM, JEM-2100F, JEOL, Japan) was employed to analyze the morphology, size, and crystallinity of the samples. The surface functional groups were characterized using fourier transform infrared spectroscopy (FT-IR, IR Tracer 100, Shimadzu, Japan), spanning a range of 4000 cm^{-1} to 400 cm^{-1} using the KBr tablet method. Nitrogen adsorption–desorption isotherms were performed on ASAP 2020 HD88 from Micromeritics (USA) to assess the surface area and porosity of the as-prepared MgO-BC-x samples. The crystalline phases of MgO-BC-x samples were analyzed using X-ray diffraction (XRD) with a Miniflex 600 diffractometer (Rigaku, Japan) operated at Cu Kα radiation (λ = 1.5406 Å). To evaluate the phosphorus adsorption performance and its impact on the surface chemistry of the adsorbents, X-ray photoelectron spectroscopy (XPS, ESCALAB™ 250Xi, Micromeritics, USA) was employed. All XPS spectra were calibrated using the C 1 s peak at 284.8 eV, providing insights into the chemical states of surface-bound species under varying pH conditions.

2.8. Statistical analysis

Data processing and visualization were executed through Excel 2019 (Microsoft Corp.) and Origin 2019 (OriginLab) software platforms. For statistical validation, inter-group variance was assessed via one-way analysis of variance (ANOVA) with post-hoc LSD testing using SPSS v25.0 (IBM Corp.), adopting a parametric testing framework with α = 0.05 as the significance criterion.

3. Results and discussion

3.1. Characteristics of the MgO-BC-x adsorbents

In this study, inspired by the culinary process of using baking soda to produce soft and porous food, a novel chemical foaming strategy was developed to fabricate honeycomb-like MgO-BC at high throughput (Ouyang et al., 2016). As shown in Fig. 1a, fresh corn stalks were first immersed in solutions with different concentrations of $Mg(HCO_3)_2$, facilitating the recrystallization of the salt both on the surface and within the internal structure of the stalks as the water evaporated. During calcination, the decomposition of these salt crystals induces in-situ etching on the surface while simultaneously doping the carbon matrix with MgO. The SEM (Fig. S2a) and TEM images (Fig. S2b) reveal contrasting morphologies between corn stalks subjected to different treatments. Untreated corn stalks after calcination retain a dense, blocky particle morphology mirroring their original structure. In contrast, carbonization of $Mg(HCO_3)_2$-treated corn stalks results in a three-dimensional scaffolding framework composed of numerous granular materials due to the introduction of MgO, as depicted in Fig. 1(b-c). The increased surface roughness of MgO-BC-2 enhances its functionality, creating numerous fine pores that significantly improve its phosphate adsorption capabilities (Montakhabi et al., 2022). It was noted that the pore walls became thinner and the biochar structure transitioned from flakes and columns to a mixed porous honeycomb structure. This morphological transformation is attributed to the thermal instability of $Mg(HCO_3)_2$ at high temperatures, which leads to significant CO_2 gas generation, thereby enlarging the pore volume (He et al., 2024). However, increasing the concentration of $Mg(HCO_3)_2$ slightly decreased the average pore size, likely due to pore obstruction caused by the by-products of decomposition (Zhao and Zhu, 2007). This is supported by the significant MgO particle agglomeration on MgO-BC-3's surface, confirming the concentration-dependent structural effects. This agglomeration may impede effective contact between the active surface of the biochar and the solution, thereby reducing its reactivity and utilization efficiency.

Transmission electron microscopy characterization of MgO-BC-2 elucidated its nanostructural architecture, as demonstrated in Fig. 1d. The biochar matrix supported monodisperse MgO nanocrystals exhibiting a mean particle diameter of 70.17 ± 1.15 nm with equilibrium spatial arrangement. Crystallographic analysis through high-resolution TEM imaging (Fig. 1e inset) resolved distinct lattice spacings measuring 0.21 nm, corresponding to the (200) crystallographic plane of periclase MgO (JCPDS 45–0946), confirming the successful formation of well-defined magnesium oxide phases (Ding et al., 2022). The EDS elemental mapping under the HAADF-STEM mode confirmed the formation of MgO nanocomposites on the biochar surface, with C (33.33 wt %), O (34.59 wt%), Mg (31.3 wt%), and N (1.79 wt%) detected in the complex (Fig. 1 f).

To investigate the effect of $Mg(HCO_3)_2$ on the properties of MgO-BC, a series of characterizations were conducted. The crystal structures of MgO-BC-x were characterized by XRD. Fig. 1 g illustrates the X-ray diffraction pattern of MgO-BC-2, revealing distinct diffraction peaks at 36.94°, 42.92°, 62.30°, 74.70°, and 78.63°, which correspond to the (111), (200), (220), (311), and (222) crystallographic planes of magnesium oxide (JCPDS card No. 45–0946). This alignment confirms the successful incorporation of MgO into the biochar matrix. Combined with the EDS results (Fig. S3), we hypothesized that the irregular precipitates on the biochar surface can be identified as MgO. However, the XRD analysis of MgO-BC-x did not reveal any diffraction peaks corresponding to graphite carbon, indicating that the as-prepared biochar is amorphous. The FTIR spectrum of MgO-BC-x, shown in Fig. 1 h, exhibits a broad peak around 3700 cm^{-1} , attributed to the stretching vibrations of -OH groups. The peak in the 2700–2800 cm^{-1} range corresponds to the antisymmetric stretching vibration of C–H groups. The infrared spectrum exhibited two prominent features: (1)

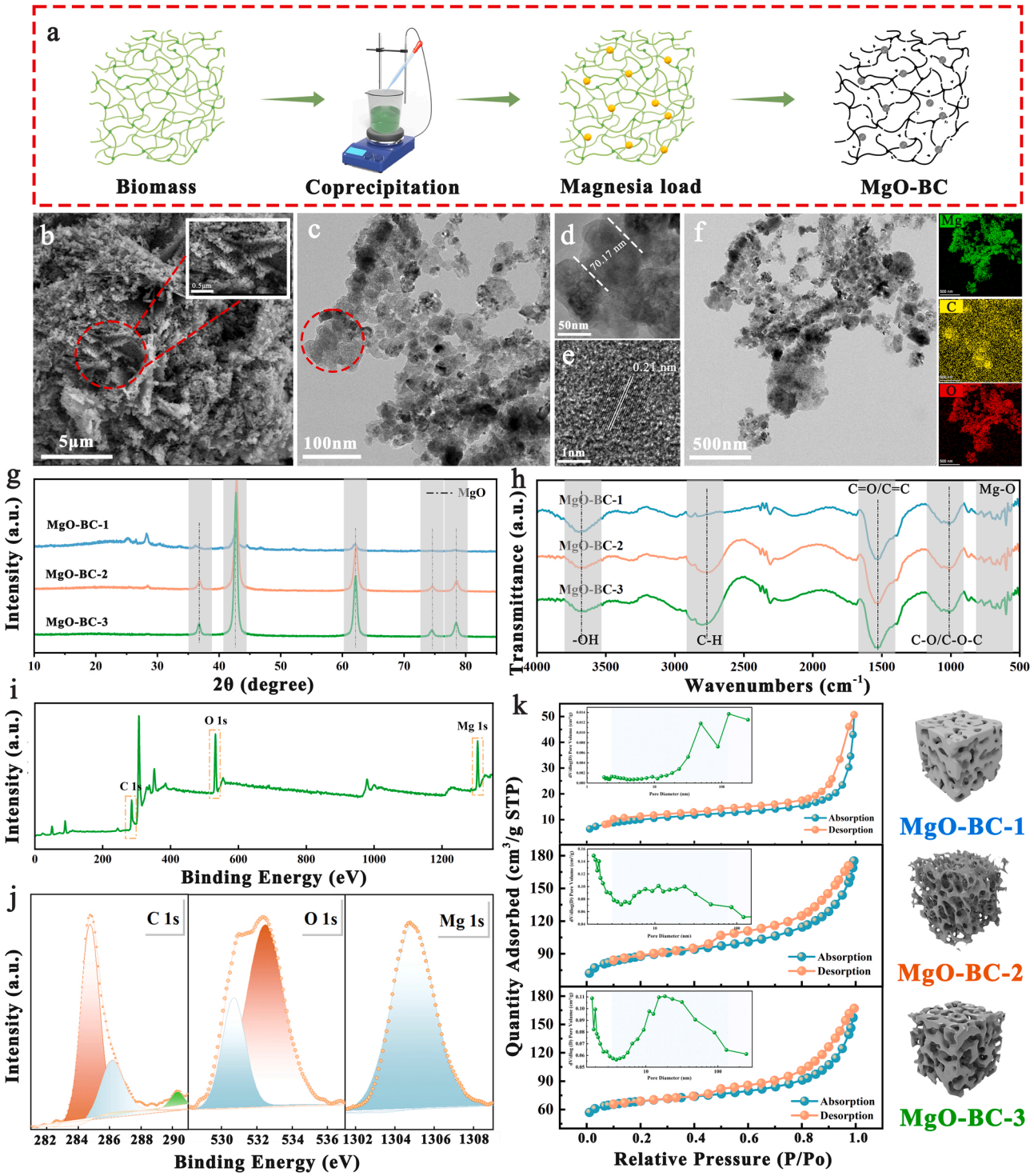

Fig. 1. (a) Diagrammatic representation of the MgO-BC-x composite preparation process. (b) SEM image, (c-d) TEM image, (e) HRTEM image of MgO-BC-2, and (f) the EDS element mappings under HAADF-STEM model. (g) XRD spectra, (h) FTIR spectra of MgO-BC-x. (i) The XPS spectrum of MgO-BC-2. High-resolution XPS spectra of C 1 s (h), O 1 s (i), and Mg 1 s (j). (k) N_2 adsorption-desorption isotherms of MgO-BC-x (inset: pore size distributions).

1400–1600 cm^{-1} absorptions indicative of conjugated carbonyl/carbon-carbon (ν(C═O/C═C)) structures, and (2) 900–1200 cm^{-1} signals characteristic of oxygen-containing moieties (ν(C-O/C-O-C)). Notably, the low-frequency region (500–800 cm^{-1}) displayed metal-oxygen vibrational modes (ν(Mg-O)), providing spectroscopic evidence for magnesium-based oxide/hydroxide species integration within the carbon matrix (Balakrishnan et al., 2020).

X-ray photoelectron spectroscopy (XPS) characterization of MgO-BC-2 revealed distinct elemental signatures in the survey spectrum (Fig. 1i), with prominent signals corresponding to carbon (C 1 s), oxygen (O 1 s), and magnesium (Mg 1 s) core levels. To elucidate surface chemical environments, high-resolution spectra were subjected to Gaussian-Lorentzian peak deconvolution. The C 1 s region (Fig. 1j) resolved three chemical states: graphitic carbon (284.8 eV), ether-type oxygen bonds (286.0 eV), and conjugated aromatic systems (290.3 eV). Parallel analysis of the O 1 s spectrum identified two dominant contributions:

hydroxyl/carbonyl oxygen (532.0 eV) and magnesium-oxide coordination (530.9 eV), demonstrating successful integration of MgO with the carbonaceous framework. Additionally, the Mg 1 s peak shows a significant feature at 1304.5 eV, attributed to native MgO. These findings highlight the significant presence of oxygen-containing functional groups and magnesium on the biochar surface, which enhance its ability to adsorb PO_4^{3-}. Furthermore, with the usage ratio of $Mg(HCO_3)_2$ increased, a shift in the elemental composition was observed, with an increase in hydrogen and decreases in carbon and nitrogen in MgO-BC-x (Table 1).

To further assess the porosity of the as-prepared carbon materials, N_2 adsorption–desorption isotherm analysis was performed and the results are depicted in Fig. 1k and Fig. S4. All the isotherm curves exhibited a typical Type IV profile, with a marked increase in the quantity of gas adsorbed at higher pressures and an H3-type hysteresis loop occurring at $p/p_0 > 0.5$. This behavior indicates capillary condensation within larger mesopores, suggesting the presence of macropores as well (Monson, 2012). The textural properties of the synthesized materials were quantified through nitrogen adsorption-desorption analysis, with surface porosity parameters derived from Brunauer-Emmett-Teller (BET) calculations (Table 1). MgO-BC-2 demonstrated superior surface development, exhibiting a BET-specific surface area of 86.36 $m^2 \cdot g^{-1}$ that exceeded values for MgO-BC-1 (35.96 $m^2 \cdot g^{-1}$) and MgO-BC-3 (69.34 $m^2 \cdot g^{-1}$). This hierarchical pore architecture suggests optimized synthesis conditions for MgO-BC-2, potentially enhancing its phosphorus adsorption capacity through increased reactive site availability. The pore volume of MgO-BC-1, MgO-BC-2 and MgO-BC-3 are 0.028 $cm^3 g^{-1}$, 0.28 $cm^3 g^{-1}$, and 0.32 $cm^3 g^{-1}$, respectively, showing an increasing trend with the dosage of $Mg(HCO_3)_2$. The mesoporous characteristics of MgO-BC composites were quantified through Barrett-Joyner-Halenda (BJH) pore network modeling, with pore size distribution profiles reconstructed from nitrogen desorption isotherms (Huang et al., 2014). The pore distribution of MgO-BC-1 ranges from 48.72 to 245.28 nm, exhibiting a macropore structure. This is attributed to the localized collapse of the material due to a small amount of CO_2, without significantly affecting the pore channels. Under CO_2-activation conditions, MgO-BC-2 and MgO-BC-3 developed tri-modal porosity, integrating micropores (<2 nm), mesopores (2–50 nm), and macropores (>50 nm) within their carbon matrices, enhances phosphate accessibility by providing molecular sieving through micropores, rapid transport via mesopores, and bulk storage in macropores, a critical design feature for sustained nutrient release in soil-water systems. This hierarchical porous structure with a high SSA can provide ample adsorption sites for the accumulation of Mg^{2+} and PO_4^{3-}, which is highly beneficial for BC. Micropores play an important role in the adsorption/desorption processes, while mesopores offer a larger accessible surface area for ion transport/charge storage. Macropores, in contrast, serve as a buffer, reducing diffusion distances to the internal surfaces of the pores. Notably, the substantial accumulation of metal salts in MgO-BC-3 caused some pore blockage, resulting in a more pronounced mesopores distribution. In summary, the introduction of magnesium bicarbonate significantly influences the characteristics of biochar. The decomposition of magnesium bicarbonate upon heating releases a substantial volume of CO_2 gas, effectively enlarging the pore size of the biochar. Simultaneously, the in-situ formation of MgO ensures its uniform distribution across the surface of the biochar. However, excessive addition of magnesium bicarbonate leads to the agglomeration of MgO, which inevitably obstructs the pores of the biochar. Considering the intended application of the synthesized samples for the adsorption of phosphates from aqueous solutions, optimizing the surface area and the MgO loading on the biochar is economically viable.

Table 1
The element content of MgO-BC-x.

	Elemental analysis				SSA(m^2/g)	V_{total} (cm^3/g)
	C %	H %	N %	S %		
MgO-BC−1	37.69	0.73	0.18	0.05	35.96	0.028
MgO-BC−2	26.24	0.85	0.09	0.04	86.36	0.28
MgO-BC−3	19.68	1.09	0.02	0	69.34	0.32

3.2. Effect adsorption of the as-prepared MgO-BC-x for adsorbents on phosphorus removal performance adsorption

Determining the optimal dosage of adsorbent is crucial for managing the operational costs of the treatment system. Generally, higher dosage of adsorbent result in greater contaminant removal efficiency (Padmavathy et al., 2016). To evaluate the effect of varying MgO-BC-x content on adsorption, we compared the adsorption properties of MgO-BC-x composites under identical conditions with different dosages. As depicted in Fig. 2a, increasing the MgO-BC-x dosage enhanced the adsorption capacity for PO_4^{3-}. Notably, MgO-BC-2 exhibited superior adsorption properties compared to MgO-BC-1 and MgO-BC-3. PO_4^{3-} concentration declined sharply from 6.46 mg/L to 0.21 mg/L as MgO-BC-2 application rates rose from 0.05 to 0.5 g/L. This observation aligns with previous research (Mahajan and Sud, 2015), which suggests that higher adsorbent quantities typically reduce the adsorption capacity per unit mass. Despite the higher quantity of MgO in the MgO-BC-3 adsorbents, their lower adsorption capacity compared to the MgO-BC-2 sample indicates that the surface structure plays a more significant role in the adsorption of phosphates. This observation suggests that the optimized structure of the adsorbent is crucial for improving adsorption efficiency, highlighting the importance of engineering the surface properties for optimal performance. In summary, the optimal concentration of $Mg(HCO_3)_2$ for preparing MgO-BC composites was found to be 0.5 mol/L. Based on its superior performance in preliminary tests, MgO-BC-2 served as the primary adsorbent in follow-up trials. Solution pH critically regulates adsorption efficiency by governing interfacial interactions between adsorbent and phosphate ions, while simultaneously controlling surface charge development. Fig. 2b presents the influence of pH on PO_4^{3-} adsorption by MgO-BC-2, showing that alkaline conditions inhibit adsorption. Under acidic conditions, the adsorption efficiency initially decreases and then increases, with the optimal removal efficiency occurring at pH 7. Consequently, a pH value of 7 was selected for further experiments. Competitive adsorption by coexisting anions (e.g., SO_4^{2-}/HCO_3^-) in phosphate-laden wastewater may compromise PO_4^{3-} capture efficiency through ionic interference. In this study, common anions found in wastewater, such as carbonate (CO_3^{2-}), sulfate (SO_4^{2-}), and chloride (Cl^-), were utilized as competing ions in a simulation to assess their influence on the adsorption capacity of MgO-BC-2. As shown in Fig. 2c and Fig. S5, the affinity of these anions for PO_4^{3-} adsorption sites follow the order $CO_3^{2-} > SO_4^{2-} > Cl^-$. The observed selectivity trend originates from variations in ionic charge magnitude and hydration shell dimensions, governing their competitive affinity toward adsorption sites. MgO-BC demonstrated a removal efficiency of 98.3 % (Fig. S6) in the treatment of real wastewater, further confirming its potential for industrial-scale application.

The temporal adsorption behavior of phosphate on MgO-BC-2 was monitored for 0–1440 min, with temporal progression profiles illustrated in Fig. 2d-f. Kinetic analysis employed four adsorption models: pseudo-first-order (Eq. 2), pseudo-second-order (Eq. 3), Elovich (Eq. 4), and intraparticle diffusion (W&M, Eq. 5) to decipher the uptake mechanism. As tabulated in Table 2, the pseudo-second-order model demonstrated optimal fitting ($R^2 = 0.9696$), confirming chemisorption as the principal phosphate uptake mechanism. This suggests the involvement of chemical bonds, electron sharing, or transfer between adsorbate and adsorbent, although physisorption may also play a minor role (Xu et al., 2024). The Elovich equation ($R^2 = 0.9637$) further validated the chemisorption mechanism through its accurate kinetic characterization.

Intraparticle diffusion analysis delineated three distinct sorption phases (Fig. 2 g): (1) rapid liquid-film diffusion of phosphate to MgO-

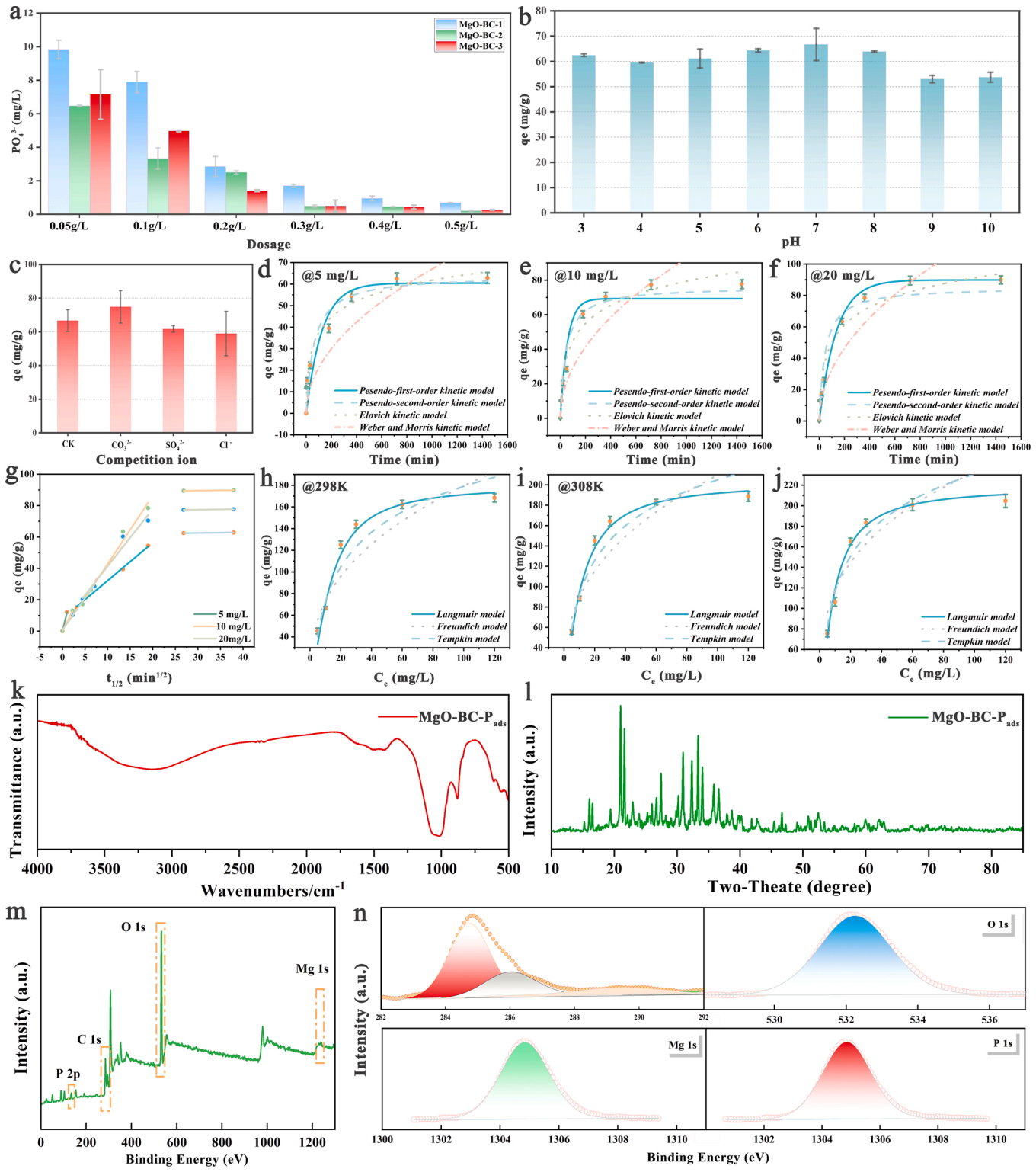

Fig. 2. Modulation effects of MgO-BC loading gradients (a), solution pH conditions (b), and coexisting anion interference (c) on phosphate adsorption performance. Kinetic of adsorption capacity of MgO-BC-2 with different PO_4^{3-} concentrations (d) 5 mg·L^{-1} (e) 10 mg·L^{-1} and (f) 20 mg·L^{-1}. Effect of contact time on adsorption capacity (g). Isotherm of adsorption capacity of PO_4^{3-} by MgO-BC-2 at different temperatures, 298 K (h), 308 K (i), and 318 K (j). The characteristic of MgO-BC-2 after adsorption. (k) FTIR spectrum. (l) XRD spectrum. (m), XPS survey spectrum, (n) high-resolution XPS spectra of C1s, O1s, Mg1s, and P 2p.

BC-2 surfaces via abundant active sites, followed by (2) gradual pore penetration, and (3) final equilibrium attainment. The second stage is the mesopore diffusion, where phosphate ions begin to diffuse into the deeper mesopores of the adsorbent as the surface sites become saturated, leading to a decrease in the diffusion rate. The final stage is the micropore equilibrium stage, where both the internal and external sites approach saturation, further slowing the diffusion rate until equilibrium is reached. Non-origin intercepts in stagewise linear regressions (Crank's diffusion theory) demonstrate that while intraparticle diffusion participates in rate control, multiple kinetic barriers coexist during phosphate

Table 2
Kinetic and Isotherm model parameters.

Kinetic model	Parameters	PO_4^{3-} concentration (mg/L)			Isotherm model	Parameters	T (K)		
		5	10	20			298	308	318
Pseudo-first-order	k_1	0.0080	0.0177	0.0074	Langmuir	q_{max} (mg/g)	189.8998	202.7459	218.3569
	q_e (mg/g)	60.4535	69.3081	89.8515		K_L (L/mg)	0.0208	0.0423	0.0625
	R^2	0.8907	0.9421	0.8637		R^2	0.9615	0.9889	0.9781
Pseudo-second-order	k_2	1.8323	2.8748	2.5877	Freundlich	K_F	29.7660	38.0819	59.7354
	q_e (mg/g)	66.3699	76.2753	85.3899		n	0.3899	0.3703	0.2952
	R^2	0.9696	0.9687	0.9386		R^2	0.8213	0.8719	0.7753
Elovich	a	2.5862	2.6657	3.2207	Tempkin	a_{te}	46.3075	49.1539	49.7160
	b	0.0871	0.0650	0.0601		b_{te}	0.4774	0.6464	1.0397
	R^2	0.9637	0.9853	0.9713		R^2	0.9131	0.9561	0.9007
W&M	k_3	2.0755	2.9233	3.2896					
	R^2	0.3519	0.8822	0.8859					

adsorption (Li et al., 2024a).

The adsorption behavior and capacity of MgO-BC-2 for PO_4^{3-} were rigorously evaluated through adsorption isotherms, employing the *Langmuir*, *Freundlich*, and *Tempkin* models. Fig. 2h-j and Table 2 demonstrate that the *Freundlich* heterogeneity parameter *(1/n)* quantifies the binding affinity between MgO-BC-2's active sites and phosphate species (Liang et al., 2021). The *Freundlich* constant K_f defines the adsorption capability of the material. Table 2 shows that the $1/n$ value for MgO-BC-2 exceeds 1, suggesting effective PO_4^{3-} removal. Furthermore, the b_t value derived from the *Temkin* equation is utilized to categorize the adsorption type. In the present study, the adsorption of PO_4^{3-} onto MgO-BC-2 seems to be of a physical nature, as evidenced by the b_t values that are lower than 4200 J/mol. The findings verified that the isotherms adhered to the Langmuir model, implying that the adsorption of PO_4^{3-} by MgO-BC-2 mainly consists of homogeneous and monolayer processes. The equilibrium constant k_L represents the intensity of the adsorption process, where a greater k_L implies a stronger adsorption ability. At a temperature of 298 K, the k_L value for the *Langmuir* model is 0.0208, and it increases to 0.0423 and 0.0625 at 308 K and 318 K, respectively. The observed positive correlation between adsorption capacity and temperature indicates an endothermic adsorption mechanism, where elevated thermal conditions promote active site accessibility and ion mobility (Al-Ghouti and Al-Absi, 2020). *Langmuir* modeling at 298 K yielded a maximum theoretical adsorption capacity of 189.90 $mg \cdot g^{-1}$. This value surpasses the capacities of other adsorbents documented in the literature (Table S2).

The thermodynamic feasibility of phosphate adsorption was systematically evaluated through analysis of Gibbs free energy (ΔG°), enthalpy (ΔH°), and entropy (ΔS°) variations. Calculated parameters demonstrated temperature-dependent adsorption behavior (Eqs. 12, 13 and 14).

In this context, T (K) signifies the temperature measured in *Kelvin*. *R* represents the gas constant, which has a value of 8.314 J·mol/K, and *Ka* refers to the adsorption equilibrium constant, with the unit being L/mol. The Gibbs free energy (ΔG°), enthalpy (ΔH°), and entropy (ΔS°) values characterizing the adsorption process are systematically compiled in Table 3, providing quantitative evidence of its temperature-dependent spontaneity and energetics. The positive ΔS value (39.0062 J/mol·K) indicates that the adsorption of PO_4^{3-} on MgO-BC-2 results in an increase the disorder or degrees of freedom. The endothermic nature of the adsorption mechanism is confirmed by the positive enthalpy change

Table 3
Thermodynamic parameters for the adsorption of MgO-BC-2.

T(K)	LangmuirVan't Hoff equation		ΔG^0(KJ/mol)	ΔH^0(KJ/mol)	ΔS^0(J/mol·K)
	q_m(mg/g)		K_a(L/mg)		
298	189.8998	114.8872	5.3610	16.9330	39.0062
308	202.7459	152.9328	4.8084	16.9330	39.0062
318	218.3569	176.3360	4.5881	16.9330	39.0062

(ΔH = 16.9330 $kJ \cdot mol^{-1}$). Gibbs free energy values (ΔG°) at 298 K, 308 K, and 318 K were calculated as 5.3610, 4.8084, and 4.5881 $kJ \cdot mol^{-1}$, respectively. The declining ΔG° values with rising temperature imply thermodynamic favorability under elevated thermal conditions, attributed to enhanced entropy-driven effects. FTIR, XRD and XPS characterization post-adsorption elucidate the mechanism behind PO_4^{3-} adsorption onto MgO-BC-2. As depicted in Fig. 2k, The FTIR spectra display notable changes in the peaks at 3700 cm^{-1}, 2700–2800 cm^{-1}, 1400–1600 cm^{-1}, and 500–800 cm^{-1}. These peaks correspond respectively to the -OH, C–H═C, C═O/C═C, and Mg-O functional groups. Such changes validate the participation of multiple functional groups in the adsorption process. Significantly, substantial fluctuations in the C═O/C═C and Mg═O peaks emphasize their importance as the main reaction sites. Moreover, the displacements of the -OH and C–H═C peaks imply their possible contribution to the reduction of PO_4^{3-}. It has been extensively reported that -OH and C–H═C can adsorb PO_4^{3-} via complexation reactions (Pradhan and Punji, 2024). The XRD patterns of MgO-BC-P_{ads} within the 2θ range from 10° to 85° are presented in Fig. 2l. Unlike the typical amorphous structure of MgO-BC-2, the pattern of MgO-BC-P_{ads} features clear crystalline peaks at 2θ = 15.95°, 16.42°, 20.93°, 21.54°, 27.35°, 30.81°, and 33.22°. These peaks can be assigned to the (020), (011), (111), (021), (130), (211), and (022) planes of the crystal structure of $KMgPO_4 \cdot 6\ H_2O$ (JCPDS card No. 35–0812), which is consistent with previous research findings (Gardner et al., 2021). XPS analysis (Fig. 2m) further corroborates these findings, revealing new photoelectron peaks corresponding to P 2p at 137.8 eV, indicating the binding of PO_4^{3-} to the surface of MgO-BC-2. The endothermic nature of the adsorption mechanism is confirmed by the positive enthalpy change (ΔH = 16.9330 $kJ \cdot mol^{-1}$). Gibbs free energy values (ΔG°) at 298 K, 308 K, and 318 K were calculated as 5.3610, 4.8084, and 4.5881 $kJ \cdot mol^{-1}$, respectively. The declining ΔG° values with rising temperature imply thermodynamic favorability under elevated thermal conditions, attributed to enhanced entropy-driven effects. The O 1 s spectra displayed a peak at 532.2 eV, associated with oxygen bonded to -C-O-. Following the adsorption of PO_4^{3-}, the area ratios of the overall oxygen groups rose from 23.28 % to 25.39 %. This increase suggests more robust interactions among the oxygen-containing functional groups. The Mg 1 s and P 2p spectra showed single peak, Mg native oxide (1304.5 eV, 11.1 %) and metal phosphate (133.0 eV, 2.48 %). After the adsorption of PO_4^{3-}, the peak area ratios of the overall Mg groups dropped from 12.84 % to 11.1 %. These XPS results complemented FTIR findings, indicating a significant reduction in Mg native oxide after adsorption, suggesting that the interaction between PO_4^{3-} and the MgO crystal through complexation reactions plays a crucial role in facilitating PO_4^{3-} adsorption, likely through adsorption/precipitation. The SEM-EDS elemental mapping further supports these findings, showing a distribution of phosphorus that closely matches that of Mg and O, confirming Mg and O are the primary adsorption sites (Fig. S7).

Kinetic models suggested that diffusion serves as the predominant mechanism that controls the transport of PO_4^{3-} onto the adsorbent

material. *Langmuir* models posited that monolayer chemisorption represents the main process facilitating the removal of PO_4^{3-} by MgO-BC-2. The adsorption of PO_4^{3-} onto MgO-BC-2 is primarily controlled by physicochemical interactions, with pore filling and surface precipitation playing key factors. The MgO-BC-2 adsorbent exhibited a notably greater adsorption capacity when compared to other adsorbents. This phenomenon can be ascribed to the larger quantity of accessible pores and Mg^{2+} ions present in MgO-BC-2. These components enhance ion exchange, interactions among functional groups, and complex precipitation processes. As Xi et al. observed, in a phosphate solution with a pH value ranging from 3 to 7, PO_4^{3-} is the dominant species (Biswas et al., 2024). The observed electron transfer mechanism between MgO-BC-2 and adsorbate species likely facilitates chemisorption. FTIR and XPS characterizations revealed enhanced oxygen-containing functional groups on MgO-BC-2, which promote phosphate (PO_4^{3-}) binding via electrostatic interactions due to the augmented density of surface-active sites (Li et al., 2022b). The presence of metallic ions facilitates physisorption, metal-ligand complexation, and pore entrapment of adsorbates (Ambaye et al., 2021). Jiang et al. observed that magnesium-modified cassava straw and banana straw biochars exhibited high saturated adsorption capacities (31.15 mg/g, TP), which were attributed to their elevated magnesium content and increased pore volume. The adsorption mechanisms in that scenario encompass surface electrostatic attraction, the precipitation of Mg^{2+} ions, and complexation with surface hydroxyl groups (Jiang et al., 2019). Consequently, this method is anticipated to remarkably enhance the accessibility of active sites for the binding of PO_4^{3-} ions to the surfaces of adsorbents, particularly under neutral pH conditions.

3.3. Effect of adsorbents on phosphorus desorption

To investigate the phosphorus release mechanism of MgO-BC-P_{ads},

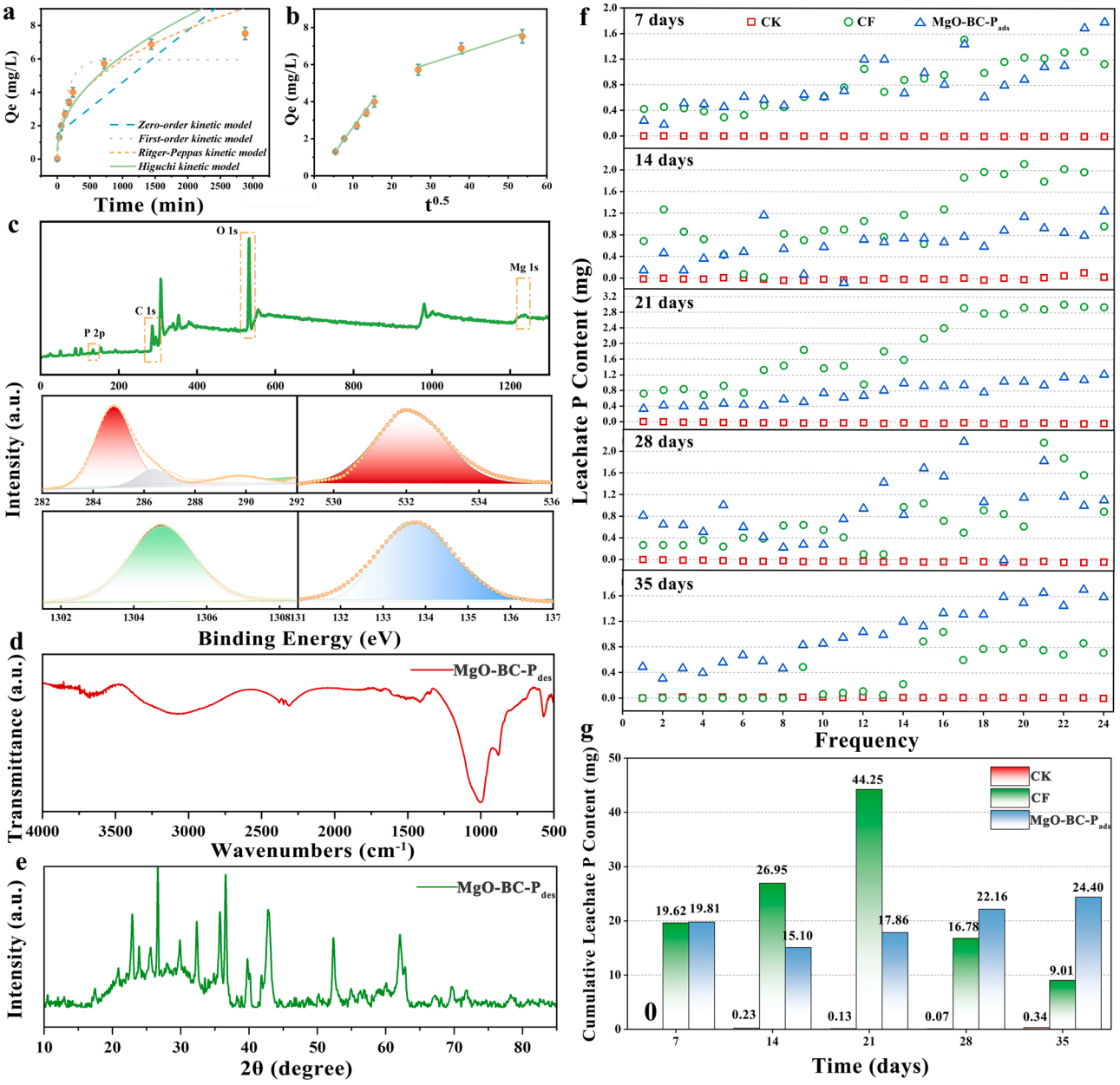

Fig. 3. Kinetic of desorption capacity of MgO-BC-P_{ads} (a), Effect of contact time on desorption capacity (b). (c) XPS survey spectrum, high-resolution XPS spectra of C1s, O1s, Mg1s, and P 2p. (d) FTIR spectrum. (e) XRD spectrum. (f) The leaching amount of PO_4^{3-} in the soil leaching solution of different treatment groups. (g) Cumulative leaching amount of PO_4^{3-} in soil leaching solution of different treatment groups.

desorption kinetic data of PO_4^{3-} were analyzed using four kinetic models (Fig. 3a), the *zero-order model* (Eq. 9), the *first-order model* (Eq. 2), the *Ritger-Peppas model* (Eq. 10), and the *Higuchi model* (Eq. 11) (Luo et al., 2024). The corresponding kinetic parameters, including the determination coefficient (R^2) and root mean squared error (RMSE), are presented in Table S3. The *Ritger-Peppas model* showed the highest R^2 value of 0.9443, with an SSR value of 11.1787. These results suggest that the *Ritger-Peppas model* provides the best fit for describing phosphorus release from MgO-BC-P_{ads} in water. The release mechanism can be classified based on the exponent *n*. When $n \leq 0.45$, *Fickian* diffusion predominates, while $0.45 < n < 0.89$ indicates non-*Fickian* diffusion, involving both nutrient diffusion and skeletal dissolution. For $n \geq 0.89$, phosphorus release slows, with skeletal dissolution being the dominant mechanism (Gao et al., 2023). The calculated *n* value for phosphorus release from MgO-BC-P_{ads} was 0.4023, indicating *Fickian* diffusion, where PO_4^{3-} diffuses from areas of higher to lower concentration. This finding supports predictions of PO_4^{3-} dispersion and dilution in the environment. Additionally, the desorption rate determined by the *first-order kinetic model* was 5.9585 mg/g, corresponding to a desorption rate of approximately 6.00 %, suggesting that physicochemical interactions are important in controlling PO_4^{3-} released from MgO-BC-P_{ads}. As depicted in Fig. 3b, phosphorus release occurs in two distinct stages. The first stage is rapid, characterized by a steep release rate, followed by a slower, gentler second stage in which phosphorus release nearly ceases. These observations are in accordance with the findings of Li et al. regarding the release of nitrogen and phosphorus from certain slow-release fertilizers (Li et al., 2022a).

Fig. 3c displays the XPS spectra of C 1 s, O 1 s, Mg 1 s, and P 2p of MgO-BC-P_{des}. Compared with MgO-BC-P_{ads}, the phosphate content in MgO-BC-P_{des} decreased from 2.48 % to 1.55 %, indicating the dissolution of surface magnesium phosphate complexes. Simultaneously, the relative content of the native Mg oxide decreased marginally from 11.1 % to 8.49 %. These findings demonstrate the biochar carrier's role in mediating Mg^{2+} ion release. The chemical state distributions of C 1 s and O 1 s for MgO-BC-2, MgO-BC-P_{ads}, and MgO-BC-P_{des}, quantified through XPS atomic percentages, are systematically compared in Table S4. When compared to MgO-BC-P_{ads}, the proportions of the C-C, C-O-C, and π-π groups in MgO-BC-P_{des} increased from 12.82 % to 14.46 %, from 0.78 % to 0.83 %, and from 0.30 % to 2.09 %, respectively. The reduction in the percentage of -C-O-C functional groups from 25.39 % to 23.40 % indicates the stability of the biochar and suggests enhanced oxidation resistance of MgO-BC-P_{ads} after Mg and P loading. This alteration in the oxygen-containing carbon groups reflects the material's ability to maintain structural integrity under oxidative conditions, thereby improving its performance in adsorption processes (Yang et al., 2016). Fig. 3d delineates the evolution of surface functional groups in MgO-BC-P_{des}. Comparative spectral analysis revealed a marked attenuation of characteristic peaks at 570.19 cm^{-1} (Mg-O vibration), 1006.13 cm^{-1} (P-O stretching), and 1435.94 cm^{-1} (C-O/C═O bonding) relative to MgO-BC-P_{ads}, suggesting phosphate-induced stabilization of reactive surface sites. This phenomenon can be ascribed to the progressive dissolution of the surface magnesium phosphate crystals. The vibrational signature of Mg-O bonds in MgO-BC-P_{des} exhibited progressive attenuation concurrent with phosphate desorption. This phenomenon aligns with the dissolution-enhancement mechanism reported by Yao et al. (Yao et al., 2013), where coexisting PO_4^{3-} and HPO_4^{-} species facilitate Mg^{2+} liberation via soluble complex formation, despite MgO's inherent thermodynamic stability in aqueous environments. Furthermore, the FTIR results revealed that there were no notable alterations in the aromatic C═H groups, nor was there the formation of new oxygen-containing groups in MgO-BC-P_{des} when compared to MgO-BC-P_{ads}. These findings imply that the improvements in the oxidation resistance of MgO-BC-P_{ads} mainly stemmed from: (1) the reduction of oxygen-containing carbon groups due to magnesium modification, and (2) the creation of a compact antioxidative barrier made up of MgO and Mg═P precipitates. This barrier avoids interference with the initial crystallization process and prolongs the slow-release period of MgO-BC-P_{ads} during soil applications. The crystal phase composition of MgO-BC-P_{des} was determined via XRD (Fig. 3e), showing typical peaks corresponding to the MgO crystal planes (200) and (220) (2θ=42.92° and 62.30°). The diffraction peak associated with $KMgPO_4{\cdot}6\,H_2O$ (JCPDS card No. 35–0812) disappeared in MgO-BC-P_{des}, indicating successful PO_4^{3-} desorption from MgO-BC-P_{ads}. The XRD peaks observed at $2\theta = 23.89°$ and 38.55° correspond to Mg_2SiO_4 (JCPDS No. 34–0189), indicating complex interfacial interactions within MgO-BC--P_{ads}, a finding corroborated by XPS data.

The persistence of MgO-BC-P_{ads} in terrestrial systems is governed by both its inherent dissolution kinetics and colloidal stability mediated through soil matrix interactions (e.g., cation exchange capacity, organic matter complexation). Fig. 3f-g illustrates changes in phosphate concentration in leachate. The application of both CF and MgO-BC-P_{ads} significantly increased the phosphate content in the soil compared to CK, suggesting that MgO-BC-P_{ads} is a promising agricultural phosphate fertilizer. The CF group exhibited extremely high PO_4^{3-} release from 7 to 21 days, peaking at 44.25 mg on day 21. The sharp release was attributed to the high solubility of superphosphate and its lack of slow-release properties (Pang et al., 2018). Following this initial surge, a more gradual phosphate release occurred between days 28 and 35. In contrast, the MgO-BC-P_{ads} group demonstrated consistent slow-release performance, with PO_4^{3-} release ranging from 15.10 to 24.40 mg over the entire 35-day leaching experiment. The increasing release of PO_4^{3-} over time can be attributed to the breakdown of biochar in the soil, which aligns with the phosphorus demand pattern for crop growth. Additionally, the distribution of PO_4^{3-} in the soil was more uniform in the MgO-BC-P_{ads} group, as evidenced by the fractional analysis of the leaching solution. Mechanistic studies have established that biochar-fertilizer composites regulate soil hydraulic properties through microstructural modification of capillary pore networks. This pore-architecture optimization effect, as evidenced by Razzaghi et al. and Das & Ghosh, creates metastable water reservoirs in interparticle voids through enhanced matric potential gradients and surface wettability modulation (Das and Ghosh, 2024; Razzaghi et al., 2020). Consequently, MgO-BC-P_{ads} can reduce the volume of leachate, limiting nutrient transport. The Chinese national standard GB/T 23348–2009 establishes guidelines for slow-release fertilizers, specifying that at 25 °C, the nutrient release rate should not exceed 15 % within 24 h and 75 % within 28 days. These thresholds are designed to regulate the controlled release of nutrients, ensuring that fertilizers do not release too quickly, which could lead to nutrient loss or environmental issues such as eutrophication. The rationale behind these percentages likely considers the solubility of nutrients and the optimal absorption rates by plants. Consequently, the MgO-BC-P_{ads} complies with these standards, showcasing remarkable slow-release performance. These results highlight MgO-BC-P_{ads} as a potential slow-release fertilizer, offering substantial promise for enhancing agricultural productivity and crop yields.

3.4. Crop growth

Phytoavailability assessments of MgO-BC-P_{ads} composites were conducted through standardized pot experiments, quantifying nutrient release kinetics and plant uptake efficiency under simulated agronomic conditions. As shown in Table 4, Fig. 4a, and Fig. S8, all fertilization treatments significantly enhanced the yield of bok choy. Significantly, when compared with the CK group, the CF group under the standard dosage showed the most substantial increase in yield. The dry weight, leaf length, and leaf number increased by 131.58 %, 14.37 %, and 57.24 %, respectively, at harvest, with these differences being statistically significant ($p < 0.05$). Similarly, MgO-BC-P_{ads} demonstrated yield-enhancing effects comparable to those of superphosphate, suggesting that MgO-BC-P_{ads} can achieve efficiencies comparable to traditional fertilizers. However, the onset of these increases was delayed. In destructive tests conducted on days 7 and 14, MgO-BC-P_{ads} did not

Table 4
Correlation index at 35 days of growth at different experimental conditions.

	CK	CF	MgO-BC-P_{ads}
Fresh weight (g)	2.92 ± 0.04	6.73 ± 2.04	8.10 ± 0.87
Dry weight (g)	0.38 ± 0.01	0.62 ± 0.12	0.88 ± 0.06
Leaf length (cm)	8.07 ± 1.40	9.73 ± 0.83	9.23 ± 0.40
Blade width (cm)	4.10 ± 0.67	5.47 ± 0.17	5.17 ± 0.29
Number of blades	7.00 ± 2.16	8.33 ± 2.05	11.00 ± 1.41
Stem length (cm)	5.80 ± 0.14	10.57 ± 0.52	9.70 ± 0.62
Root length (cm)	12.90 ± 2.25	15.60 ± 2.93	23.75 ± 5.50
Root surface area (cm^2)	2.65 ± 0.14	2.16 ± 0.07	3.81 ± 0.8
Root area (cm^2)	0.85 ± 0.05	0.69 ± 0.02	1.21 ± 0.03
Root volume (cm^3)	0.05 ± 0.004	0.03 ± 0.002	0.05 ± 0.009
Number of apexes	132.67 ± 12.26	209.33 ± 30.58	295.33 ± 7.99
Root bifurcation number	88.67 ± 4.19	91.00 ± 2.22	127.00 ± 4.60
Root crossing number	6.33 ± 0.48	5.33 ± 0.311	10.67 ± 0.52

outperform the CK group and even resulted in delayed germination (Table S5). This is consistent with previous studies, where the rapid release of PO_4^{3-} from MgO-BC-P_{ads} induced early-stage osmotic stress, including soil acidification and elevated EC, both of which delayed seed germination and growth (Li et al., 2022a). Despite this delay in germination by 2 and 3 days due to nutritional competition, the excellent slow-release performance of MgO-BC-P_{ads} compensated for this initial disadvantage. Between days 14 and 35, the MgO-BC-P_{ads} group demonstrated enhanced growth rates and greater yields when compared to the CK group. At the time of harvest, the dry weight, leaf length, and number of leaves increased by 131.58 %, 14.37 %, and 57.14 %, respectively ($p < 0.05$).

The concentrations of available phosphorus (AP), total organic carbon (TOC), and dissolved organic carbon (DOC and 72.59 mg/kg, respectively). However, AP levels in the rhizosphere soil declined rapidly after day 14, dropping to 33.19, 28.37, 24.85 mg/kg on subsequent days, with a similar trend observed in the non-rhizosphere soil (27.76, 30.59, and 30.67 mg/kg). This decrease is attributed to the prolonged use of conventional phosphorus fertilizers, which contribute to soil crusting, phosphorus leaching, and nutrient wastage, exacerbating phosphorus depletion and water pollution. In contrast, the MgO-BC-P_{ads} improved soil structure and replenished organic matter and phosphorus, maintaining AP levels consistently above the optimal threshold. The bok choy growth peaked between days 14 and 21, leading to a decrease in AP concentrations across all groups (CK, CF, and MgO-BC-P_{ads} groups). However, the slow-release properties of MgO-BC-P_{ads} mitigates ensured an adequate and continuous supply of AP, effectively meeting the nutritional demands of bok choy. In conclusion, MgO-BC-P_{ads} alleviates the constraints of conventional phosphorus fertilizers. It achieves this by supplying a balanced and continuous nutrient delivery during the entire crop growth cycle (Bhandari et al., 2023), thus presenting an innovative method for phosphorus fertilization, and available potassium (AK) were monitored to evaluate nutrient release

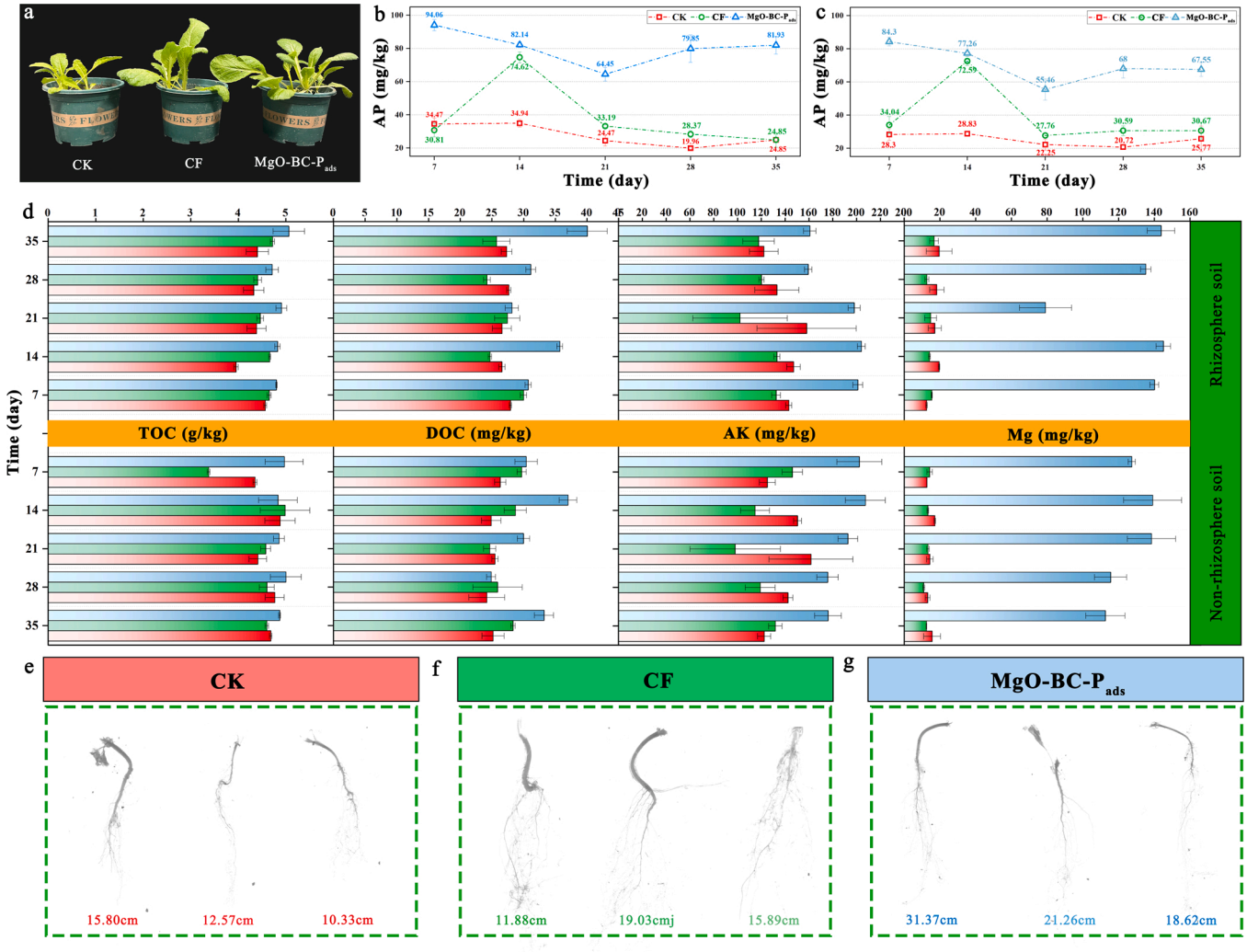

Fig. 4. Plant growth diagram (a). Change of available phosphorus content in rhizosphere soil (b) and non-rhizosphere soil (c). Changes of TOC, DOC, AK and Mg contents between rhizosphere soil and non-rhizosphere soil (d). Root scan of bok choy in different treatment groups (e-g).

and availability following the application of superphosphate and MgO-BC-P_{ads} into the soil, as shown in Fig. 4b-c and Table S6. The AP content in both rhizosphere and non-rhizosphere soil of the CF group peaked on the day 14 (74.62 mg/kg).

The influence of fertilization on DOC in soil is illustrated in Fig. 4d. Fertilization, particularly with MgO-BC-P_{ads}, led to a notable increase in DOC levels in the soil. Specifically, the DOC level rose by 46.62 % and 31.97 % in the rhizosphere and non-rhizosphere soil, respectively. This increase can be primarily attributed to the substantial carbon content in the biochar. In particular, the unique hierarchical micropore-mesopore-macropore structure of MgO-BC-P_{ads} plays a key role in carbon fixation, facilitating the adsorption of carbon in the soil, thus transforming MgO-BC-P_{ads} into an effective medium for carbon storage (Xiao et al., 2018). Consequently, MgO-BC-P_{ads} caused the most pronounced increase in DOC levels. However, it did not significantly impact TOC content in the soil, likely due to the reduced carbon retention capacity of biochar after pyrolysis at 750 ℃.

The MgO-BC-P_{ads} also positively influenced the release of AK in the soil. Compared to the CK group, the concentrations of AK in soil treated with MgO-BC-P_{ads} increased by 31.69 % and 43.87 % in the rhizosphere and non-rhizosphere soil, respectively ($P < 0.05$). Previous studies have shown that biochar can enhance potassium retention within its structure, thereby increasing the availability of potassium for plants uptake (Bilias et al., 2023; Li et al., 2024b). The mechanisms behind include increased potassium retention due to the high cation exchange capacity, porosity, and specific surface area of biochar, as well as the direct supply of potassium through K-rich biochar produced by specialized techniques. Thus, MgO-BC-P_{ads} proves to be a viable source of potassium for crops, offering both agronomic and economic benefits. Additionally, MgO-BC-P_{ads} releases significant amounts of Mg^{2+} into the soil (79.03 – 143.73 mg/kg), which positively affects the chlorophyll content of bok choy and promotes seeding growth. Co-loading MgO and phosphate species within the biochar framework establishes synergistic interactions that concurrently boost carbon stabilization and fertilizer utilization. MgO-BC-P_{ads} optimizes fertilizer preservation through three pathways: (1) ameliorating soil physicochemical characteristics, (2) stimulating microbial metabolism, and (3) prolonging phosphate bioavailability. This integrated mechanism compensates inherent nutrient limitations in pristine biochar while elevating agricultural productivity through controlled nutrient release kinetics. To further evaluate the impact of MgO-BC-P_{ads} on bok choy growth, we quantitatively measured root development. As shown in Fig. 4e-g and Table 4, MgO-BC-P_{ads} significantly enhance the total root length and root surface area of bok choy compared to the CK and CF groups, with root lengths reaching 23.75 cm, and surface areas up to 3.81 cm^2. Roots perform critical functions, such as anchoring plant and absorbing and transporting nutrients and water. The application of MgO-BC-P_{ads} increased the total root length, root volume, and root dry weight of bok choy, thereby expanding the active absorption area and improving the efficiency of resource utilization. This improvement is attributed to the impact of MgO-BC-P_{ads} on soil pore volume, structure, rhizosphere soil microbial properties, and the migration of secondary metabolites, all of which influence root growth.

A growing body of research highlights the importance of selecting appropriate modification technologies to ensure the environmental sustainability of fertilizers. An et al. engineered a coated biochar-fertilizer composite through synergistic pyrolysis-coating methods, achieving sustained phosphate release (1.14 g/L) with 35.21 % mineralization over 60 days (An et al., 2021). Nevertheless, the required polysaccharide binders (sodium alginate/starch/cellulose) introduce exogenous polymers that alter soil matrix composition. Additionally, the interactions between controlled-release fertilizers and soil nutrients, microorganisms, and moisture are intricate, influencing the distribution, release, and transformation of these fertilizers in the soil. Phosphorus mobilization in biochar-fertilizer systems was augmented by Liu et al. via phosphate-solubilizing microbial inoculation, though this biostimulation strategy induces perturbations in indigenous microbial communities (Liu et al., 2023). Yu et al. developed biomass-clay co-pyrolysis methodology yielding structurally stabilized biochar, though multistep fabrication protocols limit industrial scalability (Yu et al., 2021). The chemical foaming technology to produce MgO-BC, effectively addresses these challenges, aligning with circular economy principles and sustainable agriculture by enhancing resource, reducing environmental impact utilization, and improving soil health.

3.5. Potential risks and practical limitations for field application

This study innovatively developed a "chemical foaming method" for preparing magnesium oxide-modified biochar (MgO-BC). By utilizing the spontaneous CO_2 release during $Mg(HCO_3)_2$ pyrolysis, we simultaneously achieved optimization of the material's pore structure and uniform dispersion of MgO nanoparticles, effectively overcoming the long-standing challenge of coordinating "metal loading" with "pore regulation" in conventional modification methods. Compared with traditional impregnation methods, this approach avoids pore blockage and MgO agglomeration caused by using large anion salts, while obtaining high specific surface area materials without requiring additional activating agents. Experimental results demonstrate that the prepared MgO-BC exhibits a PO_4^{3-} adsorption capacity of 189.90 mg/g, representing a 169 % improvement over conventional $MgCl_2$-modified biochar (Chen et al., 2023). Relative to existing technologies such as ball-milling for nano-MgO preparation or microwave-hydrothermal synthesis of ternary composites, our method accomplishes both spontaneous pore creation and nano-confinement effects through a one-step pyrolysis process. Importantly, the entire preparation procedure generates no toxic byproducts, better aligning with the principles of green chemistry and circular agriculture. This breakthrough not only significantly enhances material performance but also provides an environmentally sustainable pathway for large-scale production of functional biochar materials.

While this study has demonstrated the technical feasibility of MgO-BC for phosphate recovery and slow-release fertilizer applications, we must acknowledge several crucial limitations regarding real-world wastewater treatment and agricultural implementation.

The current research, conducted under simulated wastewater conditions, revealed the modified biochar's high-capacity phosphate adsorption characteristics. However, in practical applications, the presence of high concentrations of heavy metal cations (e.g., Cd^{2+}, Pb^{2+}) in actual wastewater may compete for adsorption sites through ion exchange or coprecipitation mechanisms. Furthermore, long-term field application may introduce additional complexities, as soil acidification and root exudates could potentially alter heavy metal speciation and mobility, leading to unforeseen release risks.

Regarding potential secondary pollution from recycled products, it is important to note that our pot experiments employed simulated desorption solutions to prepare slow-release fertilizers. While this approach effectively isolated the fertilizer's nutrient delivery function from potential contaminant inputs, it does not fully represent scenarios where phosphate-laden biochar solids recovered from actual livestock wastewater are directly applied to agricultural fields.

A particularly significant knowledge gap exists concerning the fate of antibiotics present in livestock wastewater. Our current study has not systematically evaluated the potential transmission risks of these contaminants (including antibiotics and their transformation products) in soil-crop systems. This represents a critical dimension that must be addressed in future risk assessments to ensure the technology's environmental safety and practical viability. These considerations will be essential for developing comprehensive guidelines for field application and establishing appropriate regulatory frameworks.

$$q_e = V(C_1 - C_2)/m \quad (1)$$

$$q_t = q_e[1 - \exp(-k_1 t)] \quad (2)$$

$$q_t = q_e^2 k_2 t / (1 + q_e k_2 t) \quad (3)$$

$$q_t = \frac{1}{b}\ln(1 + abt) \quad (4)$$

$$q_t = k_3 t^{1/2} \quad (5)$$

$$q_e = bq_{\max} c_e / 1 + bc_e \quad (6)$$

$$q_e = k_f c_e^{1/n} \quad (7)$$

$$q_e = a_{te} \ln b_{te} c_e \quad (8)$$

$$M_t / M_\infty = K_0 t \quad (9)$$

$$M_t / M_\infty = K_{rp} t^n \quad (10)$$

$$M_t / M_\infty = K_H T^{1/2} \quad (11)$$

$$\Delta G^0 = \Delta H^0 - (-T\Delta S^0) \quad (12)$$

$$\Delta G^0 = -RT\ln K_L \quad (13)$$

$$\ln K_L = \left(-\Delta H^0 / R\right) / T + \Delta S^0 / R \quad (14)$$

4. Conclusion

The synthesis of MgO-BC utilized an innovative foaming synthesis protocol, where maize stalk provided the carbon matrix while magnesium bicarbonate served dual functions as porogen and magnesium donor. This methodology concurrently resolves dual environmental challenges: aquatic phosphate contamination and phosphate rock depletion. The MgO-BC demonstrated a substantial phosphorus adsorption capacity, with a maximum theoretical value of 189.90 mg/g, highlighting its effectiveness in capturing phosphorus from wastewater. Pseudo-second-order kinetics optimally modeled the adsorption chronology, demonstrating process control through chemisorption mechanisms involving biochar surface charge attraction (electrostatic) and ligand-exchange coordination. Field and laboratory tests confirmed that MgO-BC is capable of releasing the absorbed phosphorus into the soil. Kinetic profiling elucidated that MgO-BC-P_{ads}' sustained nutrient release originates from two coupled processes: (1) magnesium-phosphate phase dissolution and (2) biochar-mediated desorption via hierarchical porosity. This two-stage liberation pathway leads to improvements in bok choy root architecture metrics (length, volume, biomass accumulation) compared to control groups. Beyond its agricultural benefits, MgO-BC also contributes to sustainable agricultural practices and integrated waste management by converting waste biomass into a valuable resource. This method underscores the potential of MgO-BC as a sustainable solution, offering a practical application for waste biomass that aligns with environmental sustainability goals and enhances agricultural productivity. The findings emphasize the viability of MgO-BC in creating a circular economy pathway, termed biomass to biochar to biofertilizer, which significantly reduces the environmental footprint associated with conventional phosphorus fertilizers.

Compliance with ethical standards

All authors read and approved the final manuscript.

CRediT authorship contribution statement

Yu Li: Writing – original draft, Investigation. **Meiling Zhang:** Writing – original draft, Investigation. **Xianghui Meng:** Validation, Investigation. **Shuang Ai:** Investigation. **Zhuqing Liu:** Funding acquisition. **Jianghao Cheng:** Validation, Investigation. **Kui Cheng:** Writing – review & editing, Supervision, Funding acquisition. **Fan Yang:** Supervision, Funding acquisition.

Declaration of Competing Interest

The authors declare that they have no known competing financial interests or personal relationships that could have appeared to influence the work reported in this paper.

Acknowledgments

This study was funded by the National Key Research and Development Program of China (2023YFD1701604), the Outstanding Youth Project of Heilongjiang Province (JQ2024D001) the financial support from Longjiang Scholars for young scientist and Heilongjiang Provincial Undergraduate Institutions Support Plan for Outstanding Young Teachers in Fundamental Research (YQGH2023191).

Appendix A. Supporting information

Supplementary data associated with this article can be found in the online version at doi:10.1016/j.indcrop.2025.121596.

Data availability

The data that has been used is confidential.

References

Al-Ghouti, M.A., Al-Absi, R.S., 2020. Mechanistic understanding of the adsorption and thermodynamic aspects of cationic methylene blue dye onto cellulosic olive stones biomass from wastewater. Sci. Rep. 10, 15928. https://doi.org/10.1038/s41598-020-72996-3.

Almanassra, I.W., Mckay, G., Kochkodan, V., Atieh, M.A., Al-Ansari, T., 2021. A state of the art review on phosphate removal from water by biochars. Chem. Eng. J. 409, 128211. https://doi.org/10.1016/j.cej.2020.128211.

Ambaye, T.G., Vaccari, M., van Hullebusch, E.D., Amrane, A., Rtimi, S., 2021. Mechanisms and adsorption capacities of biochar for the removal of organic and inorganic pollutants from industrial wastewater. Int. J. Environ. Sci. Technol. 18, 3273–3294. https://doi.org/10.1007/s13762-020-03060-w.

An, X., Wu, Z., Qin, H., Liu, X., He, Y., Xu, X., Li, T., Yu, B., 2021. Integrated co-pyrolysis and coating for the synthesis of a new coated biochar-based fertilizer with enhanced slow-release performance. J. Clean. Prod. 283. https://doi.org/10.1016/j.jclepro.2020.124642.

Bacelo, H., Pintor, A.M., Santos, S.C., Boaventura, R.A., Botelho, C.M., 2020. Performance and prospects of different adsorbents for phosphorus uptake and recovery from water. Chem. Eng. J. 381, 122566. https://doi.org/10.1016/j.cej.2019.122566.

Balakrishnan, G., Velavan, R., Mujasam Batoo, K., Raslan, E.H., 2020. Microstructure, optical and photocatalytic properties of MgO nanoparticles. Results Phys. 16, 103013. https://doi.org/10.1016/j.rinp.2020.103013.

Bhandari, M., Kharkwal, S., Prajapati, S.K., 2023. Recycling drinking water RO reject for microalgae-mediated resource recovery. Resour. Conserv Recycl. 188, 106699. https://doi.org/10.1016/j.resconrec.2022.106699.

Bilias, F., Kalderis, D., Richardson, C., Barbayiannis, N., Gasparatos, D., 2023. Biochar application as a soil potassium management strategy: a review. Sci. Total Environ. 858, 159782. https://doi.org/10.1016/j.scitotenv.2022.159782.

Biswas, B., Adhikari, S., Jahromi, H., Ammar, M., Baltrusaitis, J., Torbert, A., Linhoss, J., Lamba, J., 2024. Magnesium doped biochar for simultaneous adsorption of phosphate and nitrogen ions from aqueous solution. Chemosphere 358, 142130. https://doi.org/10.1016/j.chemosphere.2024.142130.

Cao, D., Cao, W., Fang, J., Cai, L., 2014. Nitrogen and phosphorus losses from agricultural systems in China: a meta-analysis. Mar. Pollut. Bull. 85, 727–732. https://doi.org/10.1016/j.marpolbul.2014.05.041.

Chen, D., Cen, K., Zhuang, X., Gan, Z., Zhou, J., Zhang, Y., Zhang, H., 2022. Insight into biomass pyrolysis mechanism based on cellulose, hemicellulose, and lignin: evolution of volatiles and kinetics, elucidation of reaction pathways, and characterization of gas, biochar and bio-oil. Combust. Flame 242. https://doi.org/10.1016/j.combustflame.2022.112142.

Chen, J., Tang, S., Yan, F., Zhang, Z., 2020. Efficient recovery of phosphorus in sewage sludge through hydroxylapatite enhancement formation aided by calcium-based additives. Water Res. 171, 115450. https://doi.org/10.1016/j.watres.2019.115450.

Chen, D., Yin, Y., Xu, Y., Liu, C., 2023. Adsorptive recycle of phosphate by MgO-biochar from wastewater: Adsorbent fabrication, adsorption site energy analysis and long-

term column experiments. J. Water Process Eng. 51, 103445. https://doi.org/10.1016/j.jwpe.2022.103445.
Cordell, D., Drangert, J.-O., White, S., 2009. The story of phosphorus: global food security and food for thought. Glob. Environ. Chang. 19, 292–305. https://doi.org/10.1016/j.gloenvcha.2008.10.009.
Dai, Y., Wang, W., Lu, L., Yan, L., Yu, D., 2020. Utilization of biochar for the removal of nitrogen and phosphorus. J. Clean. Prod. 257, 120573. https://doi.org/10.1016/j.jclepro.2020.120573.
Das, S.K., Ghosh, G.K., 2024. Soil hydro-physical properties affected by biomass-derived biochar and organic manure: a low-cost technology for managing acidic mountain sandy soils of north eastern region of India. Biomass. Convers. Bioref. 14, 6621–6635. https://doi.org/10.1007/s13399-022-03107-7.
Ding, B., Ding, M., Ma, Y., Song, G., Li, Z., Ge, J., Yang, W., Wen, C., 2022. Effect of MgO on electrochemical properties of silicon-based anode composite material. Solid State Sci. 131, 106940. https://doi.org/10.1016/j.solidstatesciences.2022.106940.
Gao, F., Ye, L., Mu, X., Xu, L., Shi, Z., Luo, Y., 2023. Synergistic effects of earthworms and cow manure under reduced chemical fertilization modified microbial community structure to mitigate continuous cropping effects on Chinese flowering cabbage. Front. Microbiol. 14. https://doi.org/10.3389/fmicb.2023.1285464.
Gardner, L.J., Walling, S.A., Lawson, S.M., Sun, S., Bernal, S.A., Corkhill, C.L., Provis, J. L., Apperley, D.C., Iuga, D., Hanna, J.V., Hyatt, N.C., 2021. Characterization of and structural insight into struvite-K, $MgKPO_4{\cdot}6H_2O$, an analogue of struvite. Inorg. Chem. 60, 195–205. https://doi.org/10.1021/acs.inorgchem.0c02802.
Gilbert, N., 2009. Environment: the disappearing nutrient. Nature 461, 716–718. https://doi.org/10.1038/461716a.
Guida, S., Rubertelli, G., Jefferson, B., Soares, A., 2021. Demonstration of ion exchange technology for phosphorus removal and recovery from municipal wastewater. Chem. Eng. J. 420, 129913. https://doi.org/10.1016/j.cej.2021.129913.
He, Z.-W., Li, A.-H., Tang, C.-C., Zhou, A.-J., Liu, W., Ren, Y.-X., Li, Z., Wang, A., 2024. Biochar regulates anaerobic digestion: Insights to the roles of pore size. Chem. Eng. J. 480, 148219. https://doi.org/10.1016/j.cej.2023.148219.
He, Q., Zhao, H., Teng, Z., Wang, Y., Li, M., Hoffmann, M.R., 2022. Phosphate removal and recovery by lanthanum-based adsorbents: a review for current advances. Chemosphere 303, 134987. https://doi.org/10.1016/j.chemosphere.2022.134987.
Hu, Z., Wu, R., Pang, X., Yu, C., Jian, X., 2023. Adsorption of phosphorus in water by metal-modified large-size biochar: realizing the recovery and recycling of phosphorus. Sustain Chem. Pharm. 36, 101279. https://doi.org/10.1016/j.scp.2023.101279.
Huang, B., Bartholomew, C.H., Woodfield, B.F., 2014. Improved calculations of pore size distribution for relatively large, irregular slit-shaped mesopore structure. Microporous Mesoporous Mater. 184, 112–121. https://doi.org/10.1016/j.micromeso.2013.10.008.
Huang, Y., Zhang, D., Cheng, H., He, Y., Hu, G., 2024. Effective removal and recovery of phosphorus using ZnAl-COOH-modified biochar via hydrogen bonds. Sep. Purif. Technol. 329. https://doi.org/10.1016/j.seppur.2023.125159.
Izadi, P., Izadi, P., Eldyasti, A., 2020. Design, operation and technology configurations for enhanced biological phosphorus removal (EBPR) process: a review. Rev. Environ. Sci. Bio 19, 561–593. https://doi.org/10.1007/s11157-020-09538-w.
Jiang, Y.-H., Li, A.-Y., Deng, H., Ye, C.-H., Wu, Y.-Q., Linmu, Y.-D., Hang, H.-L., 2019. Characteristics of nitrogen and phosphorus adsorption by Mg-loaded biochar from different feedstocks. Bioresour. Technol. 276, 183–189. https://doi.org/10.1016/j.biortech.2018.12.079.
Jiao, G.-J., Ma, J., Li, Y., Jin, D., Ali, Z., Zhou, J., Sun, R., 2021. Recent advances and challenges on removal and recycling of phosphate from wastewater using biomass-derived adsorbents. Chemosphere 278, 130377. https://doi.org/10.1016/j.chemosphere.2021.130377.
Joseph, S., Cowie, A.L., Van Zwieten, L., Bolan, N., Budai, A., Buss, W., Cayuela, M.L., Graber, E.R., Ippolito, J.A., Kuzyakov, Y., 2021. How biochar works, and when it doesn't: A review of mechanisms controlling soil and plant responses to biochar. Gcb Bioenergy 13, 1731–1764. https://doi.org/10.1111/gcbb.12885.
Li, H., Li, Y., Xu, Y., Lu, X., 2020. Biochar phosphorus fertilizer effects on soil phosphorus availability. Chemosphere 244, 125471. https://doi.org/10.1016/j.chemosphere.2019.125471.
Li, J., Liu, Y., Liu, J., Cui, X., Hou, T., Cheng, D., 2022a. A novel synthetic slow release fertilizer with low energy production for efficient nutrient management. Sci. Total Environ. 831, 154844. https://doi.org/10.1016/j.scitotenv.2022.154844.
Li, N., Wang, Y., Cheng, X., Dai, H., Yan, B., Chen, G., Hou, La, Wang, S., 2022b. Influences and mechanisms of phosphate ions onto persulfate activation and organic degradation in water treatment: a review. Water Res 222, 118896. https://doi.org/10.1016/j.watres.2022.118896.
Li, Y., Xu, Y., Zhu, J., Meng, X., Ai, S., Zhang, M., Yang, F., Yin, H., Cheng, K., 2024a. Immobilization nitrogen-doped sodium alginate-derived carbon quantum dots on sodium alginate hydrogel for enhanced Pb(II) removal. Diam. Relat. Mater., 111576 https://doi.org/10.1016/j.diamond.2024.111576.
Li, Y., Zhang, M., Wang, X., Ai, S., Meng, X., Liu, Z., Yang, F., Cheng, K., 2024b. Synergistic enhancement of cadmium immobilization and soil fertility through biochar and artificial humic acid-assisted microbial-induced calcium carbonate precipitation. J. Hazard. Mater. 476, 135140. https://doi.org/10.1016/j.jhazmat.2024.135140.
Liang, H.X., Li, Y.Y., Zhao, X.K., Gao, C.L., Zhang, H.W., Geng, Z.C., She, D., 2022. Efficient Cr(VI) removal from wastewater by $D^{(+)}$-xylose based adsorbent: key roles of three-dimensional porous structures and oxygen groups. J. Hazard. Mater. 437, 108665. https://doi.org/10.1016/j.jhazmat.2022.129345.
Liang, H.X., Zhang, H.W., Zhao, P.Y., Zhao, X.K., Sun, H.W., Geng, Z.C., She, D., 2021. Synthesis of a novel three-dimensional porous carbon material and its highly selective Cr(VI) removal in wastewater. J. Clean. Prod. 306, 127204. https://doi.org/10.1016/j.jclepro.2021.127204.
Liu, Z., Wu, Z., Tian, F., Liu, X., Li, T., He, Y., Li, B., Zhang, Z., Yu, B., 2023. Phosphate-solubilizing microorganisms regulate the release and transformation of phosphorus in biochar-based slow-release fertilizer. Sci. Total Environ. 869. https://doi.org/10.1016/j.scitotenv.2023.161622.
Luo, Z., Li, Y., Pei, X., Woon, K.S., Liu, M., Lin, X., Hu, Z., Li, Y., Zhang, Z., 2024. A potential slow-release fertilizer based on biogas residue biochar: nutrient release patterns and synergistic mechanism for improving soil fertility. Environ. Res. 252, 119076. https://doi.org/10.1016/j.envres.2024.119076.
Luo, D., Wang, L., Nan, H., Cao, Y., Wang, H., Kumar, T.V., Wang, C., 2023. Phosphorus adsorption by functionalized biochar: a review. Environ. Chem. Lett. 21, 497–524. https://doi.org/10.1007/s10311-022-01519-5.
Ma, H., Gao, X., Chen, Y., Zhu, J., Liu, T., 2021. Fe (II) enhances simultaneous phosphorus removal and denitrification in heterotrophic denitrification by chemical precipitation and stimulating denitrifiers activity. Environ. Pollut. 287, 117668. https://doi.org/10.1016/j.envpol.2021.117668.
Ma, J.Z., Xia, M.Z., Zhu, S.D., Wang, F.Y., 2020. A new alendronate doped HAP nanomaterial for Pb^{2+}, Cu^{2+} and Cd^{2+} effect absorption. J. Hazard. Mater. 400, 123143. https://doi.org/10.1016/j.jhazmat.2020.123143.
Mahajan, G., Sud, D., 2015. Remediation of Cd(II) metal ion from aqueous systems by using calcium alginate modified (CAM) acacia saligna and delbergia sisso pods composite beads. Sep. Sci. Technol. 50, 354–364. https://doi.org/10.1080/01496395.2014.973512.
Monson, P.A., 2012. Understanding adsorption/desorption hysteresis for fluids in mesoporous materials using simple molecular models and classical density functional theory. Microporous Mesoporous Mater. 160, 47–66. https://doi.org/10.1016/j.micromeso.2012.04.043.
Montakhabi, F., Poursaeidi, E., Rahimi, J., Sigaroodi, M.R.J., 2022. Investigation of the effect of BC layer surface roughness and TC layer porosity on stress values in plasma sprayed coatings based on SEM images. Mater. Today Commun. 33, 104737. https://doi.org/10.1016/j.mtcomm.2022.104737.
Ouyang, T., Cheng, K., Gao, Y., Kong, S., Ye, K., Wang, G., Cao, D., 2016. Molten salt synthesis of nitrogen doped porous carbon: a new preparation methodology for high-volumetric capacitance electrode materials. J. Mater. Chem. A 4, 9832–9843. https://doi.org/10.1039/C6TA02673G.
Ownby, M., Desrosiers, D.-A., Vaneeckhaute, C., 2021. Phosphorus removal and recovery from wastewater via hybrid ion exchange nanotechnology: a study on sustainable regeneration chemistries. npj Clean. Water 4, 6. https://doi.org/10.1038/s41545-020-00097-9.
Padmavathy, K.S., Madhu, G., Haseena, P.V., 2016. A study on effects of pH, adsorbent dosage, time, initial concentration and adsorption isotherm study for the removal of hexavalent chromium (Cr (VI)) from wastewater by magnetite nanoparticles. Procedia Technol. 24, 585–594. https://doi.org/10.1016/j.protcy.2016.05.127.
Pang, W., Hou, D., Wang, H., Sai, S., Wang, B., Ke, J., Wu, G., Li, Q., Holtzapple, M., 2018. Preparation of microcapsules of slow-release NPK compound fertilizer and the release characteristics. J. Braz. Chem. Soc. 29. https://doi.org/10.21577/0103-5053.20180117.
Peng, Y., Luo, Y., Li, Y., Azeem, M., Li, R., Feng, C., Qu, G., Ali, E.F., Hamouda, M.A., Hooda, P.S., Rinklebe, J., Smith, K., Zhang, Z., Shaheen, S.M., 2023. Effect of corn pre-puffing on the efficiency of MgO-engineered biochar for phosphorus recovery from livestock wastewater: mechanistic investigations and cost benefit analyses. Biochar 5. https://doi.org/10.1007/s42773-023-00212-2.
Piash, K.S., Anwar, R., Shingleton, C., Erwin, R., Lin, L.S., Sanyal, O., 2022. Integrating chemical precipitation and membrane separation for phosphorus and ammonia recovery from anaerobic digestate. AlChE J. 68, e17869. https://doi.org/10.1002/aic.17869.
Pradhan, C., Punji, B., 2024. Iron-Catalyzed Functionalization of Heterocycles Through C—H Activation. In: Maiti, D., Sharma, U. (Eds.), Functionalisation of Heterocycles through Transition Metal Catalyzed C-H Activation. Topics in Heterocyclic Chemistry, 60. Springer, Cham. https://doi.org/10.1007/7081_2024_74.
Razzaghi, F., Obour, P.B., Arthur, E., 2020. Does biochar improve soil water retention? A systematic review and meta-analysis. Geoderma 361, 114055. https://doi.org/10.1016/j.geoderma.2019.114055.
Reinhard, C.T., Planavsky, N.J., Gill, B.C., Ozaki, K., Robbins, L.J., Lyons, T.W., Fischer, W.W., Wang, C., Cole, D.B., Konhauser, K.O., 2017. Evolution of the global phosphorus cycle. Nature 541, 386. https://doi.org/10.1038/nature20772.
Shakoor, M.B., Ye, Z.-L., Chen, S., 2021. Engineered biochars for recovering phosphate and ammonium from wastewater: a review. Sci. Total Environ. 779, 146240. https://doi.org/10.1016/j.scitotenv.2021.146240.
Wang, T., Camps-Arbestain, M., Hedley, M., Bishop, P., 2012. Predicting phosphorus bioavailability from high-ash biochars. Plant Soil 357, 173–187. https://doi.org/10.1007/s11104-012-1131-9.
Wang, J.L., Guo, X., 2020. Adsorption kinetic models: physical meanings, applications, and solving methods. J. Hazard. Mater. 390, 122156. https://doi.org/10.1016/j.jhazmat.2020.122156.
Wang, H., Xiao, K., Yang, J., Yu, Z., Yu, W., Xu, Q., Wu, Q., Liang, S., Hu, J., Hou, H., 2020. Phosphorus recovery from the liquid phase of anaerobic digestate using biochar derived from iron− rich sludge: a potential phosphorus fertilizer. Water Res 174, 115629. https://doi.org/10.1016/j.watres.2020.115629.
Xiang, W., Zhang, X., Chen, J., Zou, W., He, F., Hu, X., Tsang, D.C., Ok, Y.S., Gao, B., 2020. Biochar technology in wastewater treatment: a critical review. Chemosphere 252, 126539. https://doi.org/10.1016/j.chemosphere.2020.126539.
Xiao, X., Chen, B., Chen, Z., Zhu, L., Schnoor, J.L., 2018. Insight into multiple and multilevel structures of biochars and their potential environmental applications: a

critical review. Environ. Sci. Technol. 52, 5027–5047. https://doi.org/10.1021/acs.est.7b06487.

Xu, Y., Li, Y., Wang, G., Zhang, M., Peng, X., Yang, F., Cheng, K., 2024. Dual-use of sodium alginate to prepare sodium algenate -derived carbon dots sodium algenate hydrogel composite for Pb^{2+} removal. Appl. Surf. Sci. 654, 159416. https://doi.org/10.1016/j.apsusc.2024.159416.

Yang, F., Zhao, L., Gao, B., Xu, X., Cao, X., 2016. The interfacial behavior between biochar and soil minerals and its effect on biochar stability. Environ. Sci. Technol. 50, 2264–2271. https://doi.org/10.1021/acs.est.5b03656.

Yao, Y., Gao, B., Chen, J., Yang, L., 2013. Engineered biochar reclaiming phosphate from aqueous solutions: mechanisms and potential application as a slow-release fertilizer. Environ. Sci. Technol. 47, 8700–8708. https://doi.org/10.1021/es4012977.

Yu, J., Wu, Z., An, X., Tian, F., Yu, B., 2021. Trace metal elements mediated co-pyrolysis of biomass and bentonite for the synthesis of biochar with high stability. Sci. Total Environ. 774. https://doi.org/10.1016/j.scitotenv.2021.145611.

Zhang, P., He, M., Huo, S., Li, F., Li, K., 2022. Recent progress in metal-based composites toward adsorptive removal of phosphate: Mechanisms, behaviors, and prospects. Chem. Eng. J. 446, 137081. https://doi.org/10.1016/j.cej.2022.137081.

Zhang, H., Liang, H., Xing, L., Ding, W., Geng, Z., Xu, C., 2023c. Cellulose-based slow-release nitrogen fertilizers: synthesis, properties, and effects on pakchoi growth. Int. J. Biol. Macromol. 244, 125413. https://doi.org/10.1016/j.ijbiomac.2023.125413.

Zhang, Y., Wang, J., Feng, Y., 2021. The effects of biochar addition on soil physicochemical properties: a review. Catena 202, 105284. https://doi.org/10.1016/j.catena.2021.105284.

Zhao, Y., Zhu, G., 2007. Thermal decomposition kinetics and mechanism of magnesium bicarbonate aqueous solution. Hydrometallurgy 89, 217–223. https://doi.org/10.1016/j.hydromet.2007.07.006.

Zhou, Y., Qin, S., Verma, S., Sar, T., Sarsaiya, S., Ravindran, B., Liu, T., Sindhu, R., Patel, A.K., Binod, P., 2021. Production and beneficial impact of biochar for environmental application: a comprehensive review. Bioresour. Technol. 337, 125451. https://doi.org/10.1016/j.biortech.2021.125451.

Zhu, D., Chen, Y., Yang, H., Wang, S., Wang, X., Zhang, S., Chen, H., 2020. Synthesis and characterization of magnesium oxide nanoparticle-containing biochar composites for efficient phosphorus removal from aqueous solution. Chemosphere 247, 125847. https://doi.org/10.1016/j.chemosphere.2020.125847.

Zhu, J., Li, M., Whelan, M., 2018. Phosphorus activators contribute to legacy phosphorus availability in agricultural soils: a review. Sci. Total Environ. 612, 522–537. https://doi.org/10.1016/j.scitotenv.2017.08.095.